Hindawi
International Journal of Energy Research
Volume 2023, Article ID 7410245, 10 pages
https://doi.org/10.1155/2023/7410245

Research Article

Infiltrated Nanofiber-Based Nanostructured Electrodes for Solid Oxide Fuel Cells

Seo Ju Kim,[1] **Mingi Choi**,[2] **Taeeun Mun**,[1] **Deok Yoon Woo**,[1] **and Wonyoung Lee**[1,3]

[1]*School of Mechanical Engineering, Sungkyunkwan University, Suwon, Gyeonggi-do 16419, Republic of Korea*
[2]*Department of Future Energy Convergence, Seoul National University of Science & Technology, Seoul 01811, Republic of Korea*
[3]*SKKU Institute of Energy Science and Technology (SIEST), Sungkyunkwan University, Suwon, Gyeonggi-do 16419, Republic of Korea*

Correspondence should be addressed to Wonyoung Lee; leewy@skku.edu

Received 16 September 2022; Revised 21 October 2022; Accepted 29 October 2022; Published 3 February 2023

Academic Editor: Tholkappiyan Ramachandran

The feasibility and opportunity of nanostructured and defect-engineered electrodes for exceptional performance and stability of solid oxide fuel cells operating at intermediate temperatures (500–700°C) are reported in this study. The electrode is designed with infiltrated $La_{0.4}Sr_{0.6}MnO_{3-\delta}$ (LSM) nanoparticles as oxygen reduction reaction catalysts on an yttria-stabilized zirconia (YSZ) nanofiber scaffold with a controlled sintering temperature of 800–1200°C for optimized nanostructures and defect concentration of the nanofiber scaffold. Nanostructured electrode with the lowest sintering temperature of 800°C exhibits ~8.1 times higher specific surface area and ~1.6 times higher oxygen vacancy concentration than that with a sintering temperature of 1200°C. The cell with a sintering temperature of 800°C demonstrates an outstanding performance of ~2.11 and 1.09 W/cm^2 at 700 and 600°C, respectively, with excellent stability for 300 h under the current density of 1.5 A/cm^2 at 750°C.

1. Introduction

Solid oxide fuel cell (SOFC) is an ecofriendly energy conversion device using hydrogen as fuel, which has high thermodynamic efficiency and high-power density without carbon emissions [1, 2]. However, high operating temperature (over 800°C) is one of the most challenging issues, causing high manufacturing and maintenance costs and thermal degradation of the material and system [3, 4]. Thus, extensive attempts have been investigated to lower the operating temperature to the intermediate temperature (IT) range (500–700°C) for widespread commercialization [5–7].

Among the various factors that hinder lowering the operating temperature, the polarization resistances at the electrodes have been the biggest hurdle since they increase exponentially as the operation temperature is lowered, dominantly contributing to the overall resistance [8–10]. One of the most promising approaches to achieve the reduction of the polarization resistances at the electrodes is to fabricate nanostructured electrodes with enlarged reaction sites and facilitated reaction kinetics, which can considerably reduce the operating temperature, while maintaining the electrochemical performance [11–13]. Recently, nanofiber-based electrodes have been fabricated by precursor-based electrospinning for expanded sites for the oxygen reduction reaction (ORR), demonstrating substantially higher peak power densities compared to powder-based electrodes [14–18]. Defect engineering, which controls the concentration and distribution of the charged defects, is another important approach that can significantly lower the activation energy for ORR, enabling the effective operation at IT range (<700°C) [19, 20]. Representatively, reducing the grain size at the surface of oxygen ion conducting electrolytes ($Y_{0.08}Zr_{0.92}O_{2-\delta}$ [YSZ] or $Gd_{0.1}Ce_{0.9}O_{2-\delta}$) can significantly increase the oxygen vacancy concentration, thereby facilitating the oxygen incorporation and charge transfer at the triple phase boundaries [21, 22]. Therefore, designing the nanostructured electrode with electrospun nanofiber-based electrolyte scaffolds and infiltrated electrode nanoparticles can be a rational strategy for enlarged reaction sites or

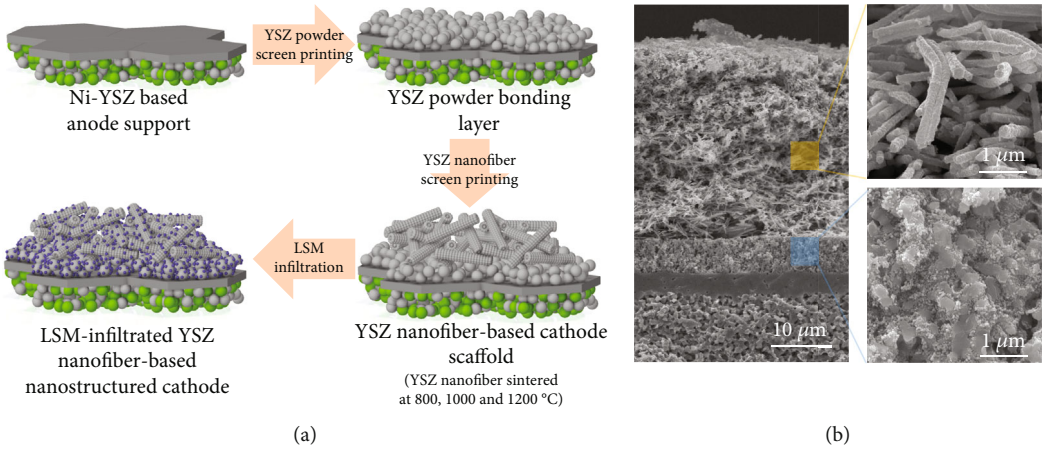

Figure 1: Fabrication process of the nanostructured cathode and cross-sectional images. (a) Illustrations of the LSM-infiltrated YSZ nanofiber-based nanostructured cathode fabrication process. (b) Cross-sectional SEM images of overall single cell with zoomed-in LSM-infiltrated YSZ nanofibers (yellow) and LSM-infiltrated YSZ powder layer (blue).

contact points between the electrolyte and electrode and to open the possibility for further engineering of defect chemistry at their interfaces [9, 10].

However, except for a few reports, this strategy has not been extensively used for SOFC electrodes, mainly because of the difficulties in nanofiber layer integration onto the electrolyte surface, resulting in poor adhesion and significant interfacial resistances [14, 23]. In general, the adhesion between two layers can be improved by sintering at high temperature for facile necking [24]. However, such high sintering temperatures can deteriorate the nanostructures and engineered defects through the agglomeration of nanoparticles to reduce the surface energy and consequent rearrangement of charged defects [4, 25, 26]. Therefore, the design and fabrication strategies to fully utilize the advantages of the nanostructured and defect-engineered electrodes while securing the sufficient adhesion between the electrolyte and electrode are essential in developing IT-SOFCs with higher performance.

In this study, we present the exceptionally high performance of IT-SOFC through the nanostructured and defect-engineered electrodes. We designed the electrode structure with infiltrated $La_{0.4}Sr_{0.6}MnO_{3-\delta}$ (LSM) nanoparticles as ORR catalysts onto the yttria-stabilized zirconia (YSZ) nanofiber scaffold. In particular, the bonding layer between the electrolyte and nanofiber scaffold enabled control of the sintering temperature in the range of 800–1200°C, thus engineering the nanostructures and defect concentration of the nanofiber scaffold, while securing sufficient adhesion. The nanostructured electrode with the lowest sintering temperature of 800°C for the nanofiber scaffold exhibited ~8.1 times the higher specific surface area and ~1.6 times higher oxygen vacancy concentration compared with those with the sintering temperature of 1200°C. Consequently, the cell with the sintering temperature of 800°C demonstrated the outstanding performance of ~2.11 and 1.09 W/cm^2 at 700 and 600°C, respectively, surpassing the previously reported YSZ electrolyte-based cells composed of the state-of-the-art cathode materials. Under the current density of 1.5 A/cm^2 at 750°C, nearly no degradation was observed for 300 h, which validates the feasibility and opportunity of the nanostructured and defect-engineered electrodes for the development of IT-SOFCs with high performance and stability.

2. Experimental

2.1. Preparation of YSZ Nanofiber. Three types of YSZ nanofibers were fabricated by the electrospinning process; 10 wt% of polyacrylonitrile (PAN, Sigma-Aldrich) was completely dissolved in N,N-dimethylformamide (DMF, Alfa Aesar) for proper viscosity of the solution at 70°C for 24 h. YSZ precursors ($Y(NO_3)_2{\cdot}6H_2O$ and $(CH_3CO_2)_xZr(OH)_y$, Sigma-Aldrich) (0.1 M) were dissolved with a certain molar ratio in the solution to form the fluorite phase of $(Y_2O_3)_{0.08}Zr_{0.92}O_{2-\delta}$. The final solution was vigorously stirred at 70°C until the complete dissolution. The fully dissolved solution was transferred into an injection pump using a 27-gauge needle (NNC-PN-27GA, NanoNC). The fiber solution was introduced with a fixed rate of 8 ml/h using a syringe pump, and an electric field of 1.5 kV/cm was adjusted with a high voltage. A grounded aluminum foil was used as the collector for the electrospun nanofibers. as-spun nanofibers were sintered with two different ramping steps. First, the ramping rate was set as 5°C/min up to 280°C. After 1 h at 280°C, the ramping rate was changed to 3°C/min up to 800, 1000, and 1200°C for 3 h, respectively.

2.2. Fabrication of Single Cells. For the electrochemical evaluation, the anode-supported cell was fabricated. NiO powder (Kojundo Chem. Lab), YSZ powder (Tosoh), and poly(methyl methacrylate) (Alfa Aesar), in a ratio of 6 : 4 : 1, were mixed into 20 ml of ethanol. Additionally, 0.3 ml of the powder dispersant, KD-6 (Croda), and the binder, polyvinyl butyral (Sigma Aldrich), was added into the solution. Then, the solution was ball-milled for 24 h. Completely dried anode powder was pressed with 40 MPa for anode support formation with a thickness of 0.5 mm using a hydraulic press and sintered at 1000°C for 3 h. The anode functional layer (AFL) and electrolyte layer were formed by spin-coating. The AFL solution was prepared

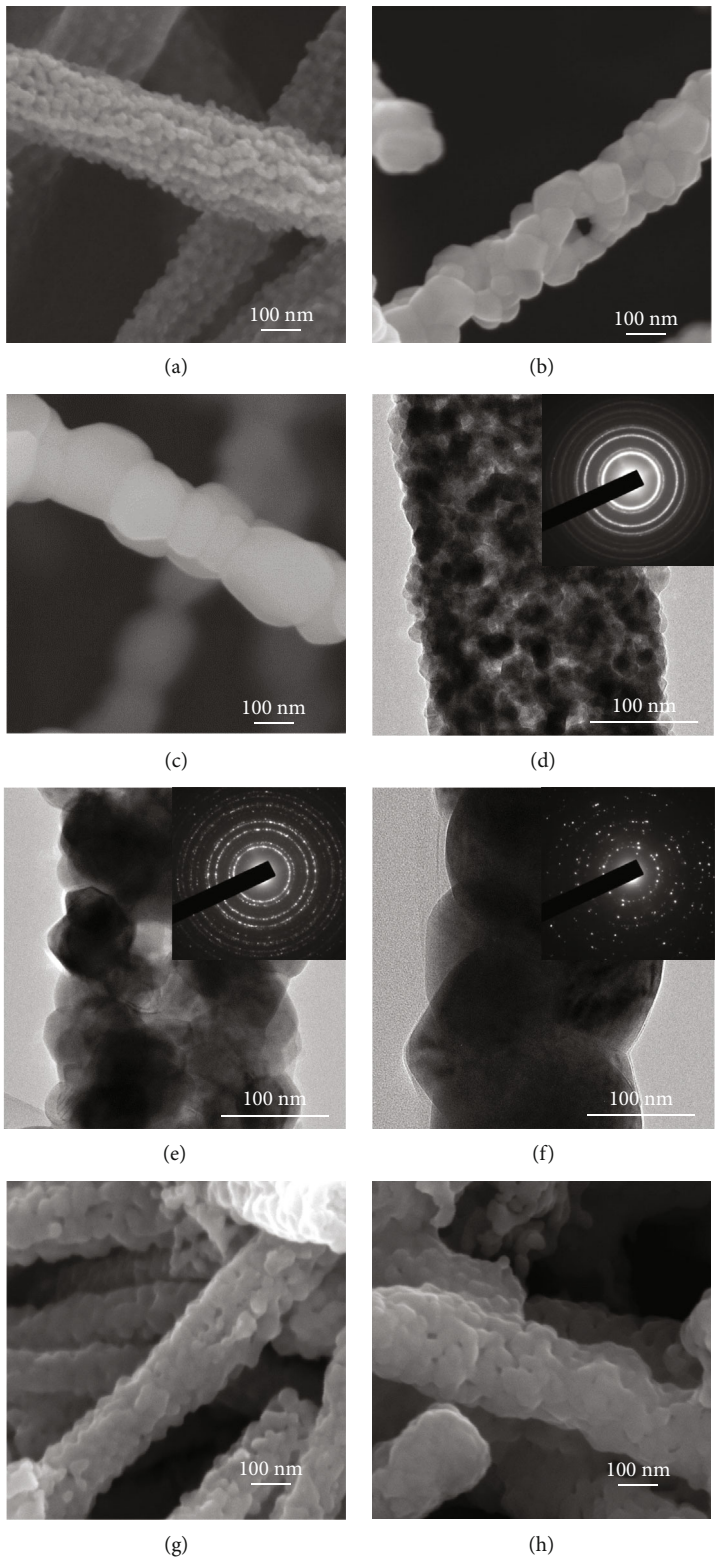

Figure 2: Continued.

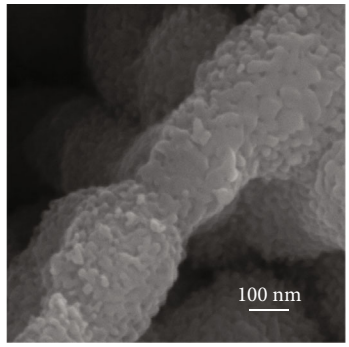

(i)

Figure 2: Surface morphologies of YSZ nanofibers and LSM-infiltrated YSZ nanofibers. SEM images of (a) NF 800, (b) NF 1000, and (c) NF 1200. TEM images of (d) NF 800, (e) NF 1000, and (f) NF 1200. SEM images of LSM-infiltrated (g) NF 800, (h) NF 1000, and (i) NF 1200.

with a mixture of NiO and YSZ powders with a 6 : 4 weight ratio dispersed into the ethanol, adding a binder, ethyl cellulose (50 cps, Sam Chun), and a dispersant, KD-6. The YSZ electrolyte solution was prepared with the same recipe using only YSZ powder. Spin-coating process was applied for the deposition of 20 μm AFL and 5 μm YSZ electrolyte layers, and they were cosintered at 1400°C for 3 h to evaporate the unnecessary organic components and obtain the dense YSZ electrolyte. For the cathode fabrication, the YSZ powder and YSZ nanofibers were deposited through the screen-printing process for a thickness of 5 μm and 30 μm, respectively. First, the YSZ powder layer for providing sufficient bonding between the YSZ nanofibers and electrolyte surface was sintered at 1200°C for 3 h. Then, the YSZ nanofibers sintered at 800, 1000, and 1200°C as composite cathode scaffold were sintered at 800°C for 3 h. To form the LSM nanoparticles onto the YSZ scaffolds, 0.6 M of LSM precursor solution was prepared. Each cation precursor ($La(NO_3)_3{\cdot}6H_2O$ (Sigma-Aldrich), $Sr(NO_3)_2$ (Sigma-Aldrich), and $Mn(NO_3)_2{\cdot}6H_2O$ (Alfa Aesar)) was dissolved in ethanol and DI-water, using a volume ratio of 5 : 5 at a molar ratio of 0.6 : 0.4 : 1. For the dispersion of the solution, Triton-X 100 (Sigma-Aldrich) was dissolved by adding 5 wt% of LSM precursor. The LSM solution, 21 μl, was dropped into the YSZ nanofiber scaffolds, to create the LSM nanoparticles using a micropipette. After the injection, the infiltrated solution was dried at 80°C for 1 h and sintered at 800°C for 3 h to form the perovskite phase of the LSM nanoparticles. Platinum paste (5542, ESL) was screen printed as the current collector in a thickness of 5 μm, followed by the sintering at 800°C for 1 h.

2.3. Characterization. In order to characterize the YSZ NF structures and fabricated electrode, scanning electron microscopy (SEM, JSM700F, JEOL) and transmission electron microscope (TEM, JEOL, JEM ARM200F) were used. Selected area electron diffraction (SAED) analysis and X-ray diffraction (XRD, Bruker Corporation, D8 Advance) with Cu Kα radiation (λ = 1.5406 Å) at 25°C (room temperature) were used to confirm the crystallinity and phase formation of the synthesized NF-based composite cathode. The specific surface area of YSZ NFs was confirmed via Brunauer-Emmett-Teller method (BET, BELSORP-mini II) with nitrogen atmosphere at a temperature of -196°C (77 K). The chemical properties were characterized using X-ray photoelectron spectroscopy (XPS, ESCA Lab 250 XPS spectrometer, VG Scientific Instruments) with a monochromatic Al K_α source. In order to evaluate the electrochemical characteristics including the electrochemical impedance spectroscopy (EIS) and current-voltage curves (I-V curves) of a single cell, a potentiostat (Interface 1010E, Gamry Instruments) was used. The single-cell test was conducted with a bias of 50 mV in a temperature range of 550–750°C and in the frequency range of 10^0–10^6 Hz. The cathode side was exposed to the ambient air, while a gas mixture of 97% H_2 and 3% H_2O with a flow rate of 100 sccm was supplied to the anode side. The electrochemical stability test was conducted with a constant current density of 1.5 A/cm^2 at 750°C for 300 h.

3. Results and Discussion

Figure 1 shows the schematics of the fabrication process of YSZ nanofiber-based NiO-YSZ anode-supported single cell and cross-sectional SEM images. The NiO-YSZ anode-supported single cell platform was fabricated by following the details in the experimental section and displayed in Figure 1(a). Onto the thin YSZ electrolyte with a thickness of ~4 μm, the porous YSZ powder scaffold in a thickness of ~6 μm was screen printed as a bonding layer with a sintering temperature of 1200°C for sufficient adhesion between the electrolyte and nanofiber-based electrode. This bonding layer is particularly important to enable the low sintering temperature for the nanofiber-based electrode; otherwise, the excessive thermal energy due to the high sintering temperature for sufficient adhesion between the electrolyte and nanofiber-based electrode substantially leads to an increase in the grain size and agglomeration, which causes the structural merits of the nanofiber-based electrodes, including the high oxygen vacancy concentration and high specific surface area, to be lost [23, 27, 28]. YSZ nanofiber scaffolds with the sintering temperature of 800, 1000, and 1200°C were deposited onto the bonding layer at a thickness of 30 μm. Thereafter, LSM precursor was infiltrated into the nanofiber scaffolds for cathodic functionalization with a sintering temperature of 800°C. Considering the typical sintering

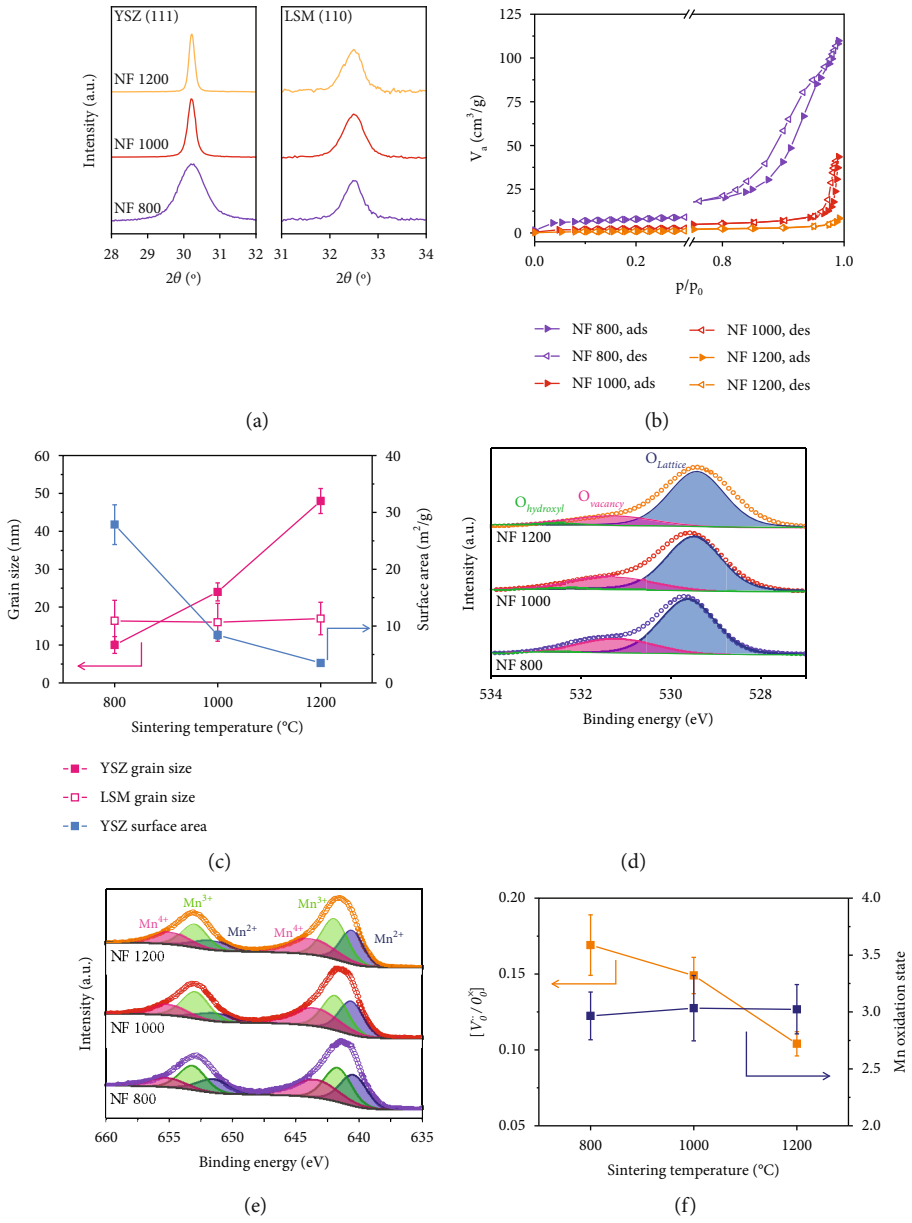

Figure 3: Structure and chemical properties of YSZ nanofibers as a function of the sintering temperature. (a) XRD patterns of YSZ (111) and LSM (110) peaks, (b) adsorbed/desorbed N_2 volume change measured by BET analysis, (c) changes in the average grain size and specific surface area as a function of the sintering temperature, (d) deconvoluted O 1s photoelectron spectra of LSM-infiltrated YSZ nanofibers, (e) deconvoluted Mn 2p photoelectron spectra of LSM-infiltrated YSZ nanofibers, and (f) changes in oxygen vacancy concentration ($[V_O^{\bullet\bullet}]/[O_O^{\times}]$) and the average Mn oxidation state as a function of the sintering temperature.

temperature of 1200°C to secure sufficient electrode necking and adhesion in the fabrication of LSM/YSZ composite electrodes, the relatively low sintering temperature of infiltrated LSM precursors of 800°C for phase formation further allows for control of the sintering temperature for the nanofiber-based electrodes from 800 to 1200°C to fully utilize the structural advantages of the nanofiber-based electrodes [29, 30]. We denoted the YSZ nanofibers with the sintering temperature of 800, 1000, and 1200°C as NF 800, NF 1000, and NF 1200, respectively.

Figure 2 shows the surface morphologies of YSZ nanofibers as a function of the sintering temperature in the range of 800–1200°C. Figures 2(a)–2(c) and 2(d)–2(f) show the SEM and TEM images of NF 800, NF 1000, and NF 1200, respectively. All nanofibers showed the solid-type structure with similar diameters of 200–250 nm. However, they showed distinct nanostructures, especially the particle size, depending on the sintering temperatures: 10–15, 30–50, and 100–130 nm for NF 800, NF 1000, and NF 1200, respectively. SAED patterns in Figures 2(d)–2(f) and Figure S1 show the continuous ring patterns in NF 800, the ring/dotted patterns in NF 1000, and the dotted patterns in NF 1200, indicating the smaller grain size with the lower sintering temperature. Figures 2(g)–2(i) show SEM images of NF 800, NF 1000, and NF 1200 after LSM infiltration, exhibiting similar surface coverage and particle size of LSM

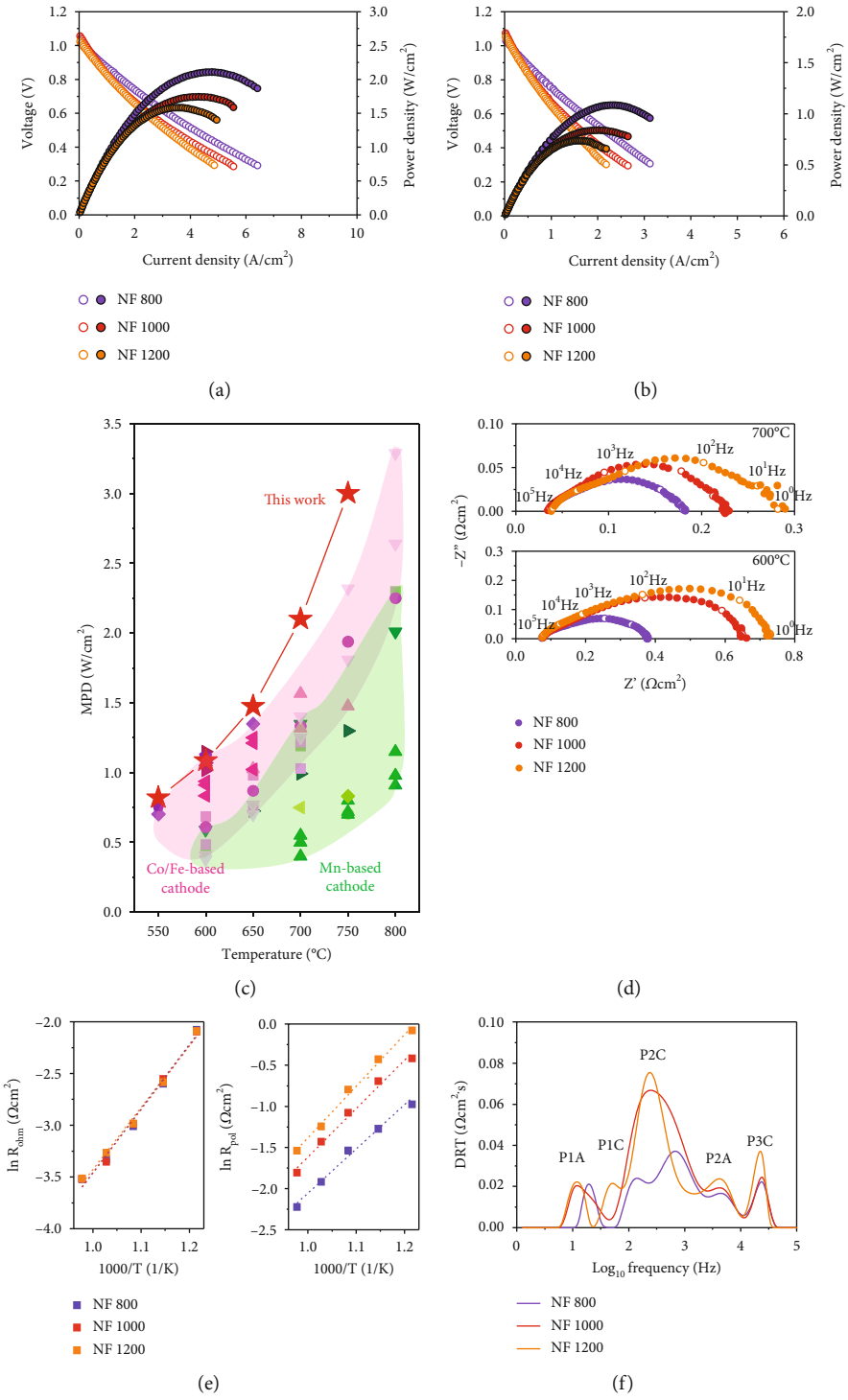

Figure 4: Continued.

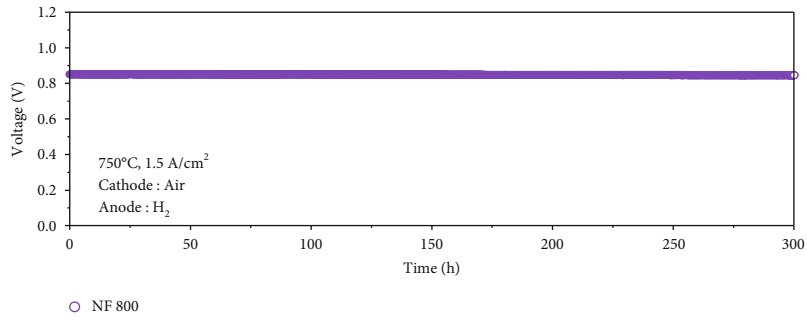

(g)

Figure 4: Electrochemical performance evaluations of LSM-infiltrated YSZ nanofiber-based nanostructured cathodes in a NiO-YSZ anode-supported single cell configuration. I-V-P curves measured at (a) 700°C and (b) 600°C, (c) MPD comparison with other reported values, (d) Nyquist curves measured at 700°C and 600°C under OCV condition, (e) Arrhenius plots for ohmic and polarization resistances, (f) DRT analysis at 700°C, and (g) galvanostatic measurement of the NF 800 cell with the constant current density of 1.5 A/cm^2 at 750°C for 300 h.

nanoparticles regardless of the sintering temperature for YSZ nanofibers. In addition, EDAX elemental mapping in Figure S2 shows the uniform dispersion of LSM nanoparticles onto YSZ nanofibers.

Figure 3 quantitatively evaluates the effects of the sintering temperature on the structural and chemical properties of the YSZ nanofibers. Figure 3(a) shows the changes in FWHM of YSZ (111) peak as a function of the sintering temperature, indicating the smaller grain size with the lower sintering temperature. Figure S3 shows the full range of XRD spectra of LSM-infiltrated YSZ nanofibers, confirming the desired phase formation of YSZ and LSM without secondary phases with the sintering temperature greater than 800°C [31]. Figure 3(b) shows the measured specific surface area of YSZ nanofibers by BET analysis through the N_2 adsorption/desorption isotherms, indicating the higher specific surface area with the lower sintering temperature [14]. Figure 3(c) quantitatively compares changes in the average grain size and specific surface area as a function of the sintering temperature, confirming the smaller grain size and larger specific surface area with the lower sintering temperature. For example, the average grain size decreased by 49% from 48.5 ± 3.3 nm in NF 1200 to 24.4 ± 2.4 nm in NF 1000 and by 79% to 10.3 ± 2.2 nm in NF 800. At the same time, the specific surface area increased by ~2.3 times from 3.43 ± 0.45 m^2/g in NF 1200 to 8.01 ± 0.72 m^2/g in NF 1,000 and by ~8.1 times to 27.86 ± 2.1 m^2/g in NF 800. Such substantial changes in structural properties can accompany changes in the chemical properties of YSZ nanofibers. In particular, oxygen vacancy concentration can be higher with the smaller grain size of YSZ nanofibers because the lattice oxygen near the grain boundaries more easily loosens the oxygen-to-metal bond than that in the grain bulk, resulting in the lower oxygen vacancy formation energy [32, 33]. Figure 3(d) shows the O 1s photoelectron spectra of YSZ nanofibers with deconvoluted three binding states of the oxygen in lattice ($O_{lattice}$), oxygen vacancy ($O_{vacancy}$), and hydroxyl group ($O_{hydroxyl}$) [34]. Figure 3(f) quantitatively compares the ratios of the fitted area of $O_{vacancy}$ to that of $O_{lattice}$, $([V_O^{\bullet\bullet}]/[O_O^{\times}])$, which can represent the oxygen vacancy concentration, as a function of the sintering temperature, confirming the higher oxygen vacancy concentration with the lower sintering temperature [21, 35, 36]. For example, the oxygen vacancy concentration increased by 30% from ~0.104 in NF 1200 to ~0.149 in NF 1000 and by 13% to ~0.169 in NF 800. In contrast to the significant changes in YSZ nanofibers, infiltrated LSM nanoparticles showed almost identical structural and chemical properties regardless of the sintering temperature for YSZ nanofibers. No noticeable difference was observed in FWHM of LSM (110) peaks in Figure 3(a), indicating the similar average grain sizes of the infiltrated LSM nanoparticles as shown in Figure 3(c). There was also no noticeable difference in Mn 2p photoelectron spectra with deconvoluted binding states of Mn^{2+}, Mn^{3+}, and Mn^{4+} in Figure 3(e), indicating the similar average oxidation states of Mn, 2.96–3.03, as shown in Figure 3(f). Therefore, we can conclude that the structural and chemical properties of YSZ nanofibers were effectively tuned by controlling the sintering temperature without changing those of infiltrated LSM nanoparticles. In particular, the lowest sintering temperature of 800°C enabled the highest specific surface area and oxygen vacancy concentration of YSZ nanofibers, which are highly desired at the interfaces between the electrode and the electrolyte for facilitated ORR kinetics [36].

We evaluated the electrochemical performance of LSM-infiltrated YSZ nanofiber-based nanostructured cathodes with a NiO-YSZ anode-supported single cell configuration in a temperature range of 550–750°C. Figures 4(a) and 4(b) demonstrate the I-V-P curves of LSM-infiltrated YSZ nanofiber-based single cells at 700 and 600°C, respectively. The maximum power densities (MPDs) of LSM-infiltrated YSZ nanofiber-based cells were substantially improved with the lower sintering temperature, exhibiting an MPD of 2.11 W/cm^2 at 700°C with NF 800 cell, which was 1.21 times higher than that of NF 1000 cell (1.74 W/cm^2) and 1.34 times higher than that of NF 1200 cell (1.58 W/cm^2). The improvement in MPD was more pronounced with the lower operating temperature. For example, NF 800 cell exhibited an MPD of 1.09 W/cm^2 at

600°C, which was 1.30 times higher than that of the NF 1000 cell (0.84 W/cm^2) and 1.47 times higher than that of the NF 1200 cell (0.74 W/cm^2). These trends, the higher MPD with the lower sintering temperature and the more improvement with the lower operating temperature, were consistent in a measured temperature range of 550–750°C as shown in Figure S4. To the best of our knowledge, the MPDs of NF 800 cell greatly surpass the previously reported values of YSZ electrolyte-based cells with LSM or YSZ/LSM as cathode materials, typically developed for operation at higher than 700°C as shown in Figure 4(c) [37–50].

The high MPD of NF 800 cell is primarily attributed to the significantly reduced electrode resistance (R_{pol}) with the lower sintering temperature for YSZ nanofiber scaffolds. Figure 4(d) shows that NF 800 cell exhibited the smallest R_{pol} of 0.15 Ωcm^2 at 700°C and 0.30 Ωcm^2 at 600°C, which were 37.5% and 47.3% smaller than those of the NF 1000 cell, 0.24 Ωcm^2 at 700°C and 0.57 Ωcm^2 at 600°C, and 48.3% and 53.8% smaller than those of the NF 1200 cell, 0.29 Ωcm^2 at 700°C and 0.65 Ωcm^2 at 600°C, respectively. Figure 4(e) shows that activation energies for R_{pol} decreased with the lower sintering temperature from 0.54 eV for NF 1200 cell to 0.52 eV for NF 1000 cell and 0.46 eV for NF 800 cell. Distribution of relaxation time (DRT) analyses, which can identify the specific frequency range of the electrochemical reactions, indicate that the improved electrode performances are mainly attributed to the facilitated ORR kinetics, especially at the interfaces between the cathode and electrolyte. Figure 4(f) shows five distinct peaks (P1A, P2A, P1C, P2C, and P3C) from DRT spectra of all cells measured at 700°C. The associated reactions with each peak are listed in Table S3 [37, 51]. The anode-related peaks (P1A and P2A) show no significant differences because the anode support, anode functional layer, and electrolyte were identically fabricated for all cells. However, the cathode-related peaks, in particular, P2C and P3C, substantially decreased with the lower sintering temperature, which correspond to charge transfer reaction and oxygen ion transport at the interfaces between infiltrated LSM nanoparticles and YSZ nanofibers, respectively. Therefore, the substantial decrease in R_{pol} of NF 800 cell can be ascribed to the structural characteristics of YSZ nanofibers enabled by the low sintering temperature: the significantly high specific surface area for extended reaction sites at the electrolyte/electrode interfaces and the high density of grain boundaries for active surface oxygen exchange due to the high concentration of oxygen vacancies. However, the ohmic resistance (R_{ohm}) remained the same as 0.04 Ωcm^2 at 700°C and 0.08 Ωcm^2 at 600°C with the same activation energies for R_{ohm} of 0.53 eV regardless of the sintering temperature, indicating no significant impact on the ion conduction due to the high density of grain boundaries, which might induce the increase in the ohmic resistance.

It should be noted that the MPDs of NF 800 cell are higher or at least comparable to those of YSZ electrolyte-based cells with state-of-the-art cathode materials such as $La_{0.6}Sr_{0.4}CoO_{3-\delta}$, $La_{0.6}Sr_{0.4}Co_{0.2}Fe_{0.8}O_{3-\delta}$, $Sm_{0.5}Sr_{0.5}CoO_{3-\delta}$, $Ba_{0.5}Sr_{0.5}Co_{0.2}Fe_{0.8}O_{3-\delta}$, and $PrBa_{0.5}Sr_{0.5}Co_{1.5}Fe_{0.5}O_{5+\delta}$, typically developed for operation below 700°C because of their high ORR activity in IT regime. However, their poor stability even below 700°C is a critical weakness to overcome [52–55]. In this concern, the excellent stability of NF 800 cell under the significantly high current density of 1.5 A/cm^2 at the high operating temperature of 750°C as shown in Figure 4(g) demonstrates its high potential for effective operation in the IT range. Therefore, our results may open opportunities for utilizing stable but less reactive materials in the IT range for high performance and stability through structural and chemical engineering with nanofiber-based electrodes.

4. Conclusion

We successfully demonstrated the significantly high performance of a NiO-YSZ anode-supported single cell by designing the electrode with LSM catalyst infiltration onto the defect-engineered YSZ nanofiber scaffold. A bonding layer between the nanofiber layer and electrolyte enabled full utilization of their beneficial characteristics while securing sufficient adhesion. We verified that lowering the sintering temperature toward 800°C exhibits ~8.1 times higher specific surface area and~1.6 times higher oxygen vacancy concentration than that sintered at 1200°C. Consequently, it demonstrated remarkable peak power densities of ~2.11 and 1.09 W/cm^2 at 700 and 600°C, respectively. More importantly, it surpasses previously reported YSZ electrolyte-based cells despite the use of the most conventional materials, YSZ and LSM. Great sustainability for 300 h at 750°C further proves the feasibility of the nanostructured and defect-engineered electrodes for IT-SOFCs with high performance and stability.

Data Availability

Data is available on request.

Conflicts of Interest

The authors declare no competing financial interest.

Authors' Contributions

Seo Ju Kim and Mingi Choi contributed equally to this work.

Acknowledgments

This work was supported by the National Research Foundation of Korea (NRF) grant funded by the Korean government (Ministry of Science and ICT, South Korea) (No. 2022R1A2C3012372, No. 2022R1A4A1031182, and No. 2021R1C1C2006657).

Supplementary Materials

Figure S1: SAED patterns of (a) NF 800, (b) NF 1000, and (c) NF 1200. Figure S2: (a) STEM image of the LSM-infiltrated YSZ nanofibers with a sintering temperature of 800°C. Elements mapping of (b) zirconia and (c) lanthanum. Figure S3: XRD patterns of (a) YSZ nanofibers with sintering temperatures of 800, 1000, and 1200°C and (b) LSM-infiltrated

YSZ nanofibers. Figure S4: MPDs of all LSM-infiltrated YSZ nanofiber cells measured in the temperature range of 550–750°C. Table S1: XPS fitting parameters of O 1s. Table S2: structural and chemical properties of YSZ nanofibers. Table S3: associated reactions with each peak in DRT spectra. *(Supplementary Materials)*

References

[1] M. B. Hanif, M. Motola, S. Rauf, C.-J. Li, and C.-X. Li, "Recent advancements, doping strategies and the future perspective of perovskite-based solid oxide fuel cells for energy conversion," *Chemical Engineering Journal*, vol. 428, article 132603, 2022.

[2] Q. Xu, Z. Guo, L. Xia et al., "A comprehensive review of solid oxide fuel cells operating on various promising alternative fuels," *Energy Conversion and Management*, vol. 253, article 115175, 2022.

[3] E. D. Wachsman and K. T. Lee, "Lowering the temperature of solid oxide fuel cells," *Science*, vol. 334, no. 6058, pp. 935–939, 2011.

[4] M. Choi and W. Lee, "Tuning the oxygen vacancy concentration in a heterostructured electrode for high chemical and electrochemical stabilities," *Chemical Engineering Journal*, vol. 431, article 134345, 2022.

[5] J. Zhang, S. Ricote, P. V. Hendriksen, and Y. Chen, "Advanced materials for thin-film solid oxide fuel cells: recent progress and challenges in boosting the device performance at low temperatures," *Advanced Functional Materials*, vol. 32, no. 22, p. 2111205, 2022.

[6] J. T. Irvine, D. Neagu, M. C. Verbraeken, C. Chatzichristodoulou, C. Graves, and M. B. Mogensen, "Evolution of the electrochemical interface in high-temperature fuel cells and electrolysers," *Nature Energy*, vol. 1, no. 1, pp. 1–13, 2016.

[7] M. Choi, J. Paik, D. Kim et al., "Exceptionally high performance of protonic ceramic fuel cells with stoichiometric electrolytes," *Energy & Environmental Science*, vol. 14, no. 12, pp. 6476–6483, 2021.

[8] S. B. Adler, "Factors governing oxygen reduction in solid oxide fuel cell cathodes," *Chemical reviews.*, vol. 104, no. 10, pp. 4791–4844, 2004.

[9] S. J. Kim, M. Choi, J. Lee, and W. Lee, "Modifying defect structures at interfaces for high-performance solid oxide fuel cells," *Journal of the European Ceramic Society*, vol. 40, no. 8, pp. 3089–3097, 2020.

[10] S. J. Kim, J. Baek, M. Choi, J. Lee, and W. Lee, "Controlling oxygen defect chemistry at electrolyte surface of intermediate temperature solid oxide fuel cells," *Journal of Power Sources*, vol. 509, p. 230351, 2021.

[11] D. Ding, X. Li, S. Y. Lai, K. Gerdes, and M. Liu, "Enhancing SOFC cathode performance by surface modification through infiltration," *Energy & Environmental Science.*, vol. 7, no. 2, pp. 552–575, 2014.

[12] M. Choi, J. Lee, and W. Lee, "Nano-film coated cathode functional layers towards high performance solid oxide fuel cells," *Journal of Materials Chemistry A*, vol. 6, no. 25, pp. 11811–11818, 2018.

[13] A. Orera, A. Betato, J. Silva-Treviño, Á. Larrea, and M. Á. Laguna-Bercero, "Advanced metal oxide infiltrated electrodes for boosting the performance of solid oxide cells," *Journal of Materials Chemistry A*, vol. 10, no. 5, pp. 2541–2549, 2022.

[14] M. Ahn, J. Lee, and W. Lee, "Nanofiber-based composite cathodes for intermediate temperature solid oxide fuel cells," *Journal of Power Sources*, vol. 353, pp. 176–182, 2017.

[15] Y. Chen, Y. Bu, Y. Zhang et al., "A highly efficient and robust nanofiber cathode for solid oxide fuel cells," *Advanced Energy Materials*, vol. 7, no. 6, p. 1601890, 2017.

[16] C. Gumeci, J. Parrondo, A. M. Hussain, D. Thompson, and N. Dale, "Praseodymium based double-perovskite cathode nanofibers for intermediate temperature solid oxide fuel cells (IT-SOFC)," *International Journal of Hydrogen Energy*, vol. 46, no. 62, pp. 31798–31806, 2021.

[17] J. Bai, Z. Han, B. Lv, X. Chen, X. Zhu, and D. Zhou, "Preparation of 3D structure high performance Ba0·5Sr0·5Fe0·8-Cu0·2O3-δ nanofiber SOFC cathode material by low-temperature calcination method," *International Journal of Hydrogen Energy*, vol. 46, no. 11, pp. 8132–8142, 2021.

[18] C. Kim, H. Park, I. Jang et al., "Morphologically well-defined $Gd_{0.1}Ce_{0.9}O_{1.95}$ embedded $Ba_{0.5}Sr_{0.5}Co_{0.8}Fe_{0.2}O_{3-\delta}$ nanofiber with an enhanced triple phase boundary as cathode for low-temperature solid oxide fuel cells," *Journal of Power Sources*, vol. 378, pp. 404–411, 2018.

[19] Y. Zhu, X. Liu, S. Jin et al., "Anionic defect engineering of transition metal oxides for oxygen reduction and evolution reactions," *Journal of Materials Chemistry A*, vol. 7, no. 11, pp. 5875–5897, 2019.

[20] S. J. Kim, J. Y. Koo, T. Mun, M. Choi, and W. Lee, "Tailoring defect chemistry at interfaces for promoted oxygen reduction reaction kinetics," *Journal of Materials Chemistry A.*, vol. 8, no. 44, pp. 23313–23322, 2020.

[21] W. Lee, H. J. Jung, M. H. Lee et al., "Oxygen surface exchange at grain boundaries of oxide ion conductors," *Advanced Functional Materials*, vol. 22, no. 5, pp. 965–971, 2012.

[22] J. S. Park, J. An, M. H. Lee, F. B. Prinz, and W. Lee, "Effects of surface chemistry and microstructure of electrolyte on oxygen reduction kinetics of solid oxide fuel cells," *Journal of Power Sources*, vol. 295, pp. 74–78, 2015.

[23] J. Lee, S. Hwang, M. Ahn et al., "Enhanced interface reactivity by a nanowrinkled functional layer for intermediate-temperature solid oxide fuel cells," *Journal of Materials Chemistry A*, vol. 7, no. 37, pp. 21120–21127, 2019.

[24] V. Wilde, H. Störmer, J. Szász, F. Wankmüller, E. Ivers-Tiffée, and D. Gerthsen, "$Gd_{0.2}Ce_{0.8}O_2$ Diffusion barrier layer between $(La_{0.58}Sr_{0.4})(Co_{0.2}Fe_{0.8})O_3$–$\delta$ Cathode and $Y_{0.16}Zr_{0.84}O_2$ Electrolyte for solid oxide fuel cells: effect of barrier layer sintering temperature on microstructure," *ACS Applied Energy Materials*, vol. 1, no. 12, pp. 6790–6800, 2018.

[25] Y. Li, W. Zhang, Y. Zheng et al., "Controlling cation segregation in perovskite-based electrodes for high electro-catalytic activity and durability," *Chemical Society Reviews*, vol. 46, no. 20, pp. 6345–6378, 2017.

[26] N. Tsvetkov, Q. Lu, L. Sun, E. J. Crumlin, and B. Yildiz, "Improved chemical and electrochemical stability of perovskite oxides with less reducible cations at the surface," *Nature Materials*, vol. 15, no. 9, pp. 1010–1016, 2016.

[27] M. Ahn, S. Han, J. Lee, and W. Lee, "Electrospun composite nanofibers for intermediate-temperature solid oxide fuel cell electrodes," *Ceramics International*, vol. 46, no. 5, pp. 6006–6011, 2020.

[28] M. Ahn, J. Cho, and W. Lee, "One-step fabrication of composite nanofibers for solid oxide fuel cell electrodes," *Journal of Power Sources*, vol. 434, article 226749, 2019.

[29] H. S. Song, W. H. Kim, S. H. Hyun, J. Moon, J. Kim, and H.-W. Lee, "Effect of starting particulate materials on microstructure and cathodic performance of nanoporous LSM-YSZ composite cathodes," *Journal of Power Sources*, vol. 167, no. 2, pp. 258–264, 2007.

[30] J. A. Cebollero, M. Laguna-Bercero, R. Lahoz, J. Silva, R. Moreno, and A. Larrea, "Optimization of laser-patterned YSZ-LSM composite cathode-electrolyte interfaces for solid oxide fuel cells," *Journal of the European Ceramic Society*, vol. 39, no. 12, pp. 3466–3474, 2019.

[31] H. He, Y. Huang, J. Regal, M. Boaro, J. M. Vohs, and R. J. Gorte, "Low-temperature fabrication of oxide composites for solid-oxide fuel cells," *Journal of the American Ceramic Society*, vol. 87, no. 3, pp. 331–336, 2004.

[32] J. Bae, Y. Lim, J.-S. Park et al., "Thermally-induced dopant segregation effects on the space charge layer and ionic conductivity of nanocrystalline gadolinia-doped ceria," *Journal of the Electrochemical Society*, vol. 163, no. 8, pp. F919–F926, 2016.

[33] D. S. Aidhy, Y. Zhang, and W. J. Weber, "Impact of segregation energetics on oxygen conductivity at ionic grain boundaries," *Journal of Materials Chemistry A*, vol. 2, no. 6, pp. 1704–1709, 2014.

[34] S. Jeong and J. Moon, "Low-temperature, solution-processed metal oxide thin film transistors," *Journal of Materials Chemistry*, vol. 22, no. 4, pp. 1243–1250, 2012.

[35] X. Guo and Z. Zhang, "Grain size dependent grain boundary defect structure: case of doped zirconia," *Acta Materialia*, vol. 51, no. 9, pp. 2539–2547, 2003.

[36] J. Y. Koo, T. Mun, J. Lee, M. Choi, S. J. Kim, and W. Lee, "Enhancement of oxygen reduction reaction kinetics using infiltrated yttria- stabilized zirconia interlayers at the electrolyte/electrode interfaces of solid oxide fuel cells," *Journal of Power Sources*, vol. 472, article 228606, 2020.

[37] X. Zhang, L. Liu, Z. Zhao et al., "Enhanced oxygen reduction activity and solid oxide fuel cell performance with a nanoparticles-loaded cathode," *Nano Letters*, vol. 15, no. 3, pp. 1703–1709, 2015.

[38] C. Ren, T. Liu, P. Maturavongsadit, J. A. Luckanagul, and F. Chen, "Effect of PEG additive on anode microstructure and cell performance of anode- supported MT-SOFCs fabricated by phase inversion method," *Journal of Power Sources*, vol. 279, pp. 774–780, 2015.

[39] Y. Jeon, J.-H. Myung, S.-H. Hyun, Y.-G. Shul, and J. T. S. Irvine, "Corn-cob like nanofibres as cathode catalysts for an effective microstructure design in solid oxide fuel cells," *Journal of Materials Chemistry A*, vol. 5, no. 8, pp. 3966–3973, 2017.

[40] T. Liu, Y. Wang, C. Ren, S. Fang, Y. Mao, and F. Chen, "Novel light-weight, high-performance anode-supported microtubular solid oxide fuel cells with an active anode functional layer," *Journal of Power Sources*, vol. 293, pp. 852–858, 2015.

[41] M. Ab Rahman, M. H. D. Othman, H. Fansuri et al., "Development of high-performance anode/electrolyte/cathode microtubular solid oxide fuel cell via phase inversion-based co-extrusion/co-sintering technique," *Journal of Power Sources*, vol. 467, article 228345, 2020.

[42] M. C. Tucker, G. Y. Lau, C. P. Jacobson, L. C. DeJonghe, and S. J. Visco, "Performance of metal-supported SOFCs with infiltrated electrodes," *Journal of Power Sources*, vol. 171, no. 2, pp. 477–482, 2007.

[43] W. Zhang, H. Wang, K. Guan et al., "$La_{0.6}Sr_{0.4}Co_{0.2}Fe_{0.8}O_3-\delta/CeO_2$ heterostructured composite nanofibers as a highly active and robust cathode catalyst for solid oxide fuel cells," *ACS Applied Materials & Interfaces*, vol. 11, no. 30, pp. 26830–26841, 2019.

[44] B.-K. Park, R. Scipioni, and S. A. Barnett, "Enhancement of $Ni–(Y_2O_3)_{0.08}(ZrO_2)_{0.92}$ fuel electrode performance by infiltration of $Ce_{0.8}Gd_{0.2}O_2-\delta$nanoparticles," *Journal of Materials Chemistry A*, vol. 8, no. 7, pp. 4099–4106, 2020.

[45] J. Kim, S. Im, S. H. Oh et al., "Naturally diffused sintering aid for highly conductive bilayer electrolytes in solid oxide cells," *Science Advances*, vol. 7, no. 40, p. eabj8590, 2021.

[46] K. Sato, C. Iwata, N. Kannari, and H. Abe, "Highly accelerated oxygen reduction reaction kinetics in colloidal-processing-derived nanostructured lanthanum strontium cobalt ferrite/gadolinium-doped ceria composite cathode for intermediate-temperature solid oxide fuel cells," *Journal of Power Sources*, vol. 414, pp. 502–508, 2019.

[47] E. O. Oh, C. M. Whang, Y. R. Lee et al., "Extremely thin bilayer electrolyte for solid oxide fuel cells (SOFCs) fabricated by chemical solution deposition (CSD)," *Advanced Materials*, vol. 24, no. 25, pp. 3373–3377, 2012.

[48] C. Kim, S. Kim, I. Jang, H. Yoon, T. Song, and U. Paik, "Facile fabrication strategy of highly dense gadolinium-doped ceria/yttria- stabilized zirconia bilayer electrolyte via cold isostatic pressing for low temperature solid oxide fuel cells," *Journal of Power Sources*, vol. 415, pp. 112–118, 2019.

[49] D.-H. Myung, J. Hong, K. Yoon et al., "The effect of an ultra-thin zirconia blocking layer on the performance of a 1-μm-thick gadolinia-doped ceria electrolyte solid-oxide fuel cell," *Journal of Power Sources*, vol. 206, pp. 91–96, 2012.

[50] J. H. Kim, J. K. Kim, H. G. Seo et al., "Ex-solved ag nanocatalysts on a Sr-free parent scaffold authorize a highly efficient route of oxygen reduction," *Advanced Functional Materials*, vol. 30, no. 27, p. 2001326, 2020.

[51] Z. Zheng, J. Jing, Z. Lei et al., "Performance and DRT analysis of infiltrated functional cathode based on the anode supported SOFCs with long-term stability," *International Journal of Hydrogen Energy*, vol. 47, no. 41, pp. 18139–18147, 2022.

[52] M. Choi, S. Kim, J. Paik, and W. Lee, "Enhanced Cr tolerance of perovskite oxide via Gd0.1Ce0.9O2 surface modifications," *Korean Journal of Chemical Engineering*, vol. 37, no. 8, pp. 1346–1351, 2020.

[53] M. Choi, I. A. M. Ibrahim, K. Kim et al., "Engineering of charged defects at perovskite oxide surfaces for exceptionally stable solid oxide fuel cell electrodes," *ACS Applied Materials & Interfaces*, vol. 12, no. 19, pp. 21494–21504, 2020.

[54] J. Y. Koo, H. Kwon, M. Ahn et al., "Suppression of Cation Segregation in $(La,Sr)CoO_3-\delta$ by Elastic Energy Minimization," *ACS Applied Materials & Interfaces*, vol. 10, no. 9, pp. 8057–8065, 2018.

[55] M. Choi, S. J. Kim, and W. Lee, "Effects of water atmosphere on chemical degradation of $PrBa_{0.5}Sr_{0.5}Co_{1.5}Fe_{0.5}O_5+\delta$ electrodes," *Ceramics International*, vol. 47, no. 6, pp. 7790–7797, 2021.